

# Efficient Vessel Feature Detection for Endoscopic Image Analysis

Bingxiong Lin, *Student Member, IEEE*, Yu Sun\*, *Senior Member, IEEE*, Jaime E. Sanchez, and Xiaoning Qian, *Member, IEEE*

**Abstract**—Distinctive feature detection is an essential task in computer-assisted minimally invasive surgery (MIS). For special conditions in an MIS imaging environment, such as specular reflections and texture homogeneous areas, the feature points extracted by general feature point detectors are less distinctive and repeatable in MIS images. We observe that abundant blood vessels are available on tissue surfaces and can be extracted as a new set of image features. In this paper, two types of blood vessel features are proposed for endoscopic images: branching points and branching segments. Two novel methods, ridgeness-based circle test and ridgeness-based branching segment detection are presented to extract branching points and branching segments, respectively. Extensive *in vivo* experiments were conducted to evaluate the performance of the proposed methods and compare them with the state-of-the-art methods. The numerical results verify that, in MIS images, the blood vessel features can produce a large number of points. More importantly, those points are more robust and repeatable than the other types of feature points. In addition, due to the difference in feature types, vessel features can be combined with other general features, which makes them new tools for MIS image analysis. These proposed methods are efficient and the code and datasets are made available to the public.

**Index Terms**—Branching point, branching segment, endoscopic image analysis, minimally invasive surgery (MIS), vessel feature detection.

## I. INTRODUCTION

**I**N minimally invasive surgery (MIS), distinctive image feature extraction is one of the fundamental tasks. The extracted image features can be used for tissue tracking [1]–[3], deformation recovery [4], [5], 3-D reconstruction [6], [7], endoscope localization [8]–[10], augmented reality [8], [10], [11], and intraoperative registration [3], [12].

Different methods have been proposed to extract image features in computer vision. Depending on what information is used, these methods can be broadly classified into three categories: intensity-based detectors, first-derivative-based detectors, and second-derivative-based detectors. The methods

in the first category directly rely on the comparison of pixel intensity. For example, in the features from accelerated segment test (FAST) [13], [14], Rosten and Drummond placed a circle at each pixel and determined that the pixel was a corner if there was a continuously bright or dark segment along the placed circle.

Methods in the second category are based on the first derivatives, namely  $I_x$ ,  $I_y$  along  $x$ - and  $y$ - coordinates in a given raw image  $I$ . Since the first derivative is proportional to the intensity change,  $I_x$  and  $I_y$  are able to capture areas with large intensity change, such as edges and boundaries of objects. To find patches that are likely to be corners, Harris and Stephens [15] exploited the eigenvalues of the autocorrelation matrix. Mikolajczyk and Schmid [16] modified the Harris corners and proposed the Harris-affine detector, which is invariant under affine transformations. To overcome the difficulty of tissue deformation in MIS images, the anisotropic feature detector (AFD) was introduced in [17].

In the third category, the second derivatives of the raw image are analyzed and used for feature detection. The second derivatives have strong responses on blobs and ridges [18]. Many of these methods compute the Hessian matrix based on the second derivatives to detect interest points. Those pixels whose determinants of the Hessian matrices were local extrema in both image space and scale space were chosen as interest points in the Hessian-affine detector [18]. As an approximation of Laplacian of Gaussian (the trace of the Hessian matrix), difference of Gaussian (DoG) [19] detected interest points as the local extreme points in both image space and scale space. Bay *et al.* approximated the Gaussian filters with box filters in the calculation of the Hessian matrix, and the obtained speeded up robust features (SURF) detector was typically faster than the DoG detector [20].

The previously introduced methods were mainly designed for general purposes, such as in images from man-made environments. On the contrary, MIS images are taken inside the human body and are quite different from the images taken in daily life. For example, MIS images contain abundant specular reflections, homogeneous areas, smokes, and so on. Much research has been presented to overcome those difficulties. Feature detectors and descriptors designed for MIS images to overcome tissue deformation were presented in [1] and [17]. Puerto-Souza and Mariottini proposed the novel hierarchical multiaffine (HMA) [21], [22] and adaptive multiaffine (AMA) [23] algorithms to improve the feature matching performance for endoscopic images. They also developed a dense feature matching method to recover the locations of image features on tissue surfaces [24]. Tissue

Manuscript received March 8, 2014; revised October 11, 2014; accepted November 9, 2014. Date of publication November 20, 2014; date of current version March 17, 2015. This work was supported by the National Science Foundation under Grant 1035594. *Asterisk indicates corresponding author.*

B. Lin is with the University of South Florida.

\*Yu Sun is with the Department of Computer Science and Engineering, University of South Florida, Tampa, FL 33620 USA (e-mail: yusun@cse.usf.edu).

J. E. Sanchez is with University of South Florida.

X. Qian is with the Texas A&M University.

This paper has supplementary material available online at <http://ieeexplore.ieee.org> (File size: 103 MB).

Color versions of one or more of the figures in this paper are available online at <http://ieeexplore.ieee.org>.

Digital Object Identifier 10.1109/TBME.2014.2373273

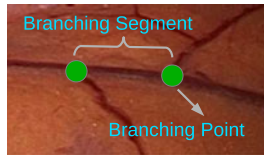


Fig. 1. Illustration of vessel features: branching point (detected by RBCT) and branching segment (detected by RBSD).

surface tracking and reconstruction for MIS have also been widely studied and different methods have been introduced to overcome the difficulties of tissue deformations and low texture [3], [4], [6], [25]. More details on the optical surface reconstruction and tissue surface tracking methods for MIS are available in [7] and [26].

The goal of this study is to design efficient algorithms that can detect robust and repeatable MIS image features across different viewpoints and different lighting conditions. It is desirable to develop a feature detector that will turn the drawbacks of the *in vivo* environment to advantages. We notice that blood vessels are abundant within the intraabdominal environment, such as on the abdominal wall and on the surface of tissue organs. The explicit extraction of blood vessels provides a large number of new types of features for MIS image analysis. Blood vessel detection is one of the fundamental research topics in image-guided surgeries and has many medical applications. For example, in neurosurgeries, Ding *et al.* estimated the cortical displacement based on blood vessel detection, and overcame the problem of brain shift and deformation caused by pressure after the open of dura [12]. In simultaneous localization and mapping (SLAM) system, blood vessels can be represented as curves and used to estimate camera motion. It has been known that curves are more robust than points in camera motion estimation [27]. Since vessels are attached to the surface of tissue surfaces and deform with the tissue, the detection of vessels are crucial to recover the tissue deformation [12]. In retinal image analysis, vessel detection and segmentation in retinal images provide important information to diagnose diseases.

Two types of blood vessel features are defined in this paper: branching points and branching segments. Bifurcations and crossing points are defined as branching points. We consider a blood vessel segment that has branching points at both ends as a branching segment. A blood vessel segment that has only one branching point is called a half branching segment. An example image with two branching points and one branching segment is shown in Fig. 1. Note that branching segments are essentially curve segments and a pair of branch segment correspondence can generate tens of pairs of point correspondences. Our previous work in [28] proposed vesselness-based circle test (VBCT) and vesselness-based branching segment detection to extract the two types of vessel features based on Frangi vesselness [29]. This study proposes a new way of blood vessel enhancement, based on a new ridgeness measure (see Section II-B), which provides more accurate vessel localizations. Based on the ridgeness representation, more robust methods of vessel feature detection are presented. Mean-

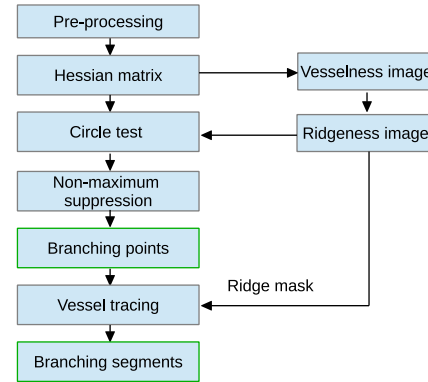


Fig. 2. Overview of the branching point and branching segment detection.

while, this study provides an in-depth analysis and thorough evaluation of the proposed methods.

## II. METHODS

A novel branching point detector, ridgeness-based circle test (RBCT), and a novel branching segment detector, ridgeness-based branching segment detection (RBSD), are introduced in this paper. The overview of our proposed vessel feature detection is shown in Fig. 2. First, image preprocessing, such as specular reflection removal, is applied on the input image. Then, Hessian matrix is calculated for each pixel, based on which Frangi vesselness and ridgeness are computed. Next, circle tests are performed to detect branching points. Last, the vessel tracing technique is introduced to detect branching segments.

### A. Detecting Candidate Branching Points

It is known that among all three channels in the RGB fundus image, the green channel provides the best contrast between vessels and the background [30]. Our experiments show that this also applies to MIS images, and hence, only the green channel is used in our method. Another special property of MIS images is the abundant specular reflections that are view-dependent, and therefore, can cause error to endoscope tracking if they are picked up as feature points. Similar to [2] and [8], the specular reflections are detected as the pixels whose intensities are larger than a global threshold. In addition, their  $3 \times 3$  neighbors are also marked as specular reflections.

The scale-space representation of an image  $I$  (green channel) is  $L(x, y, \sigma) = G(x, y; \sigma) * I(x, y)$ , where  $G(\cdot; \sigma)$  is a 2-D Gaussian function with standard deviation  $\sigma$ , and  $*$  represents convolution operation. A Hessian matrix is calculated for each pixel in each image level of the scale space, as shown in (1). Note that, in this paper, the scale space is only used during the calculation of Frangi vesselness [29] and ridgeness (see Section II-B) and all the remaining calculation is based on the single Frangi vesselness image or the ridgeness image.

$$H = \begin{bmatrix} \frac{\partial^2 L}{\partial x^2} & \frac{\partial^2 L}{\partial x \partial y} \\ \frac{\partial^2 L}{\partial y \partial x} & \frac{\partial^2 L}{\partial y^2} \end{bmatrix}. \quad (1)$$

TABLE I  
EIGENVALUES ANALYSIS TOWARD VESSEL AND BRANCHING  
POINTS ( $0 < \lambda_1 < \lambda_2$ ). L: LOW, M: MIDDLE, H: HIGH

$\lambda_1$	$\lambda_2$	pattern
L	L	background noise
L	H	dark tubular structure
M	H	branching point and spur
H	H	blob, specular reflection

The eigenvalues of the Hessian matrix are denoted as  $\lambda_1, \lambda_2$  and eigenvectors  $V_1, V_2$ . Negative eigenvalues indicate bright tubular structures and positive eigenvalues represent dark tubular structures [29]. In this study, since the vessels are dark on MIS images, the negative eigenvalues are removed and the eigenvalues are sorted so that  $0 < \lambda_1 < \lambda_2$ . It is known that the absolute values of the two eigenvalues represent the intensity variances of two orthogonal directions. The tubular structure has a small  $\lambda_1$  because the variance along the vessel direction is small. At the endpoint of a vessel, the intensity variance is large along the vessel. The branching point can be considered as the connection of three or four vessel segments, and hence, it has a larger  $\lambda_1$  than other points on the vessels. Blob has a large intensity variance in almost every direction, therefore, it has the largest  $\lambda_1$ . Similar to [29], the relationship of eigenvalues and the pixel type is summarized in Table I.

To detect bifurcations, Baboiu and Hamarneh presented three measures with similar performance:  $\lambda_1, \lambda_1 \cdot \lambda_2$  and  $1 - \exp(-2 \cdot (\lambda_1/\lambda_2)^2)$  [31]. The feature detector with the second measure is actually a variant of the aforementioned Hessian-affine detector. Those measures are sensitive to noise and have a very high false positive detection rate, because many other structures also have high responses to those measures, such as blobs, specular reflections, and spurs. Therefore, it is difficult to distinguish branching points from other structures with those measures. In this study, the candidates of branching points are defined as:  $\lambda_1 > \lambda_{1\min}$  and  $\text{Ridgeness} > R_{\min}$  for a ridgeness image that we introduce later in Section II-B. As an example, the  $\lambda_1$  image and  $\lambda_2$  image are shown, respectively, in Fig. 3(b) and (c).

### B. Blood Vessel Enhancement: Ridgeness

Based on the well-known Frangi vesselness [29], a new blood vessel enhancement technique is introduced in this section, which is referred to as ‘‘ridgeness’’ in this paper. Different from the thick representation of vessels in the Frangi vesselness, we look for ridge pixels that achieve single-pixel width. Here, the width of ridges is defined as the number of pixels in the direction of the eigenvector  $V_2$ . For completeness, the definition of the Frangi vesselness is as follows:

$$V(\sigma) = \exp\left(\frac{\lambda_1^2/\lambda_2^2}{2 \cdot \beta^2}\right) \cdot \left(1 - \exp\left(\frac{-(\lambda_1^2 + \lambda_2^2)}{(2 \cdot c^2)}\right)\right) \quad (2)$$

where  $V$  stands for Vesselness,  $\beta$  and  $c$  are soft thresholds from [29].

The ridge in a 2-D image is a good approximation of the vessel center line and has been extracted for vessel segmentation [32]. Compared with the vessels in the vesselness image, the

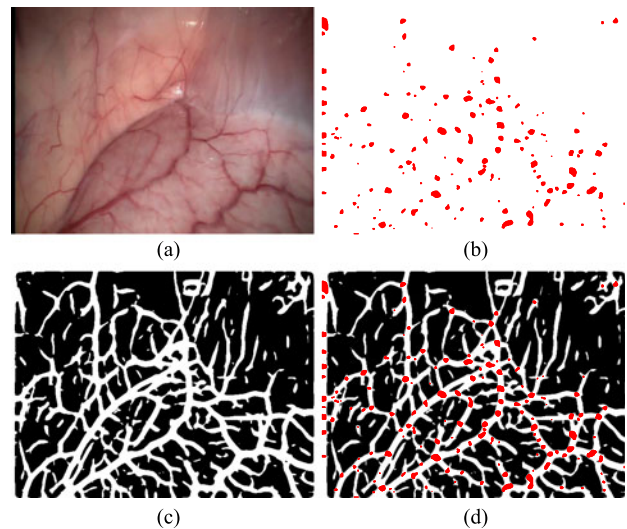


Fig. 3. Illustration of eigenvalues of Hessian matrix ( $0 < \lambda_1 < \lambda_2$ ). (a) original image. (b) binary  $\lambda_1$  image (red). (c) binary  $\lambda_2$  image (white). (d)  $\lambda_1$  image (red) overlaid on top of  $\lambda_2$  image (white). Note that for better visualization, both  $\lambda_1$  and  $\lambda_2$  have been binarized (1 for positive values and 0 for negative values)

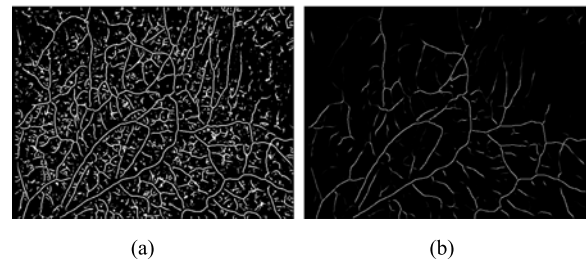


Fig. 4. Comparison of (a) binary ridge image and (b) our ridgeness image. Zooming in is recommended to see the broken branching points and single-pixel-width ridges.

ridges are thinner and clearer. In [32], ridges are defined as pixels where the first derivative of the raw image intensity changes sign in the direction of the eigenvector  $V_2$  (across the vessel). One example of the detected binary ridges based on the aforementioned definition is shown in Fig. 4(a). Since a small amount of intensity change might flip the sign of the first derivative, the aforementioned definition tends to detect massive ‘‘ridges’’ with many false positives, which include tiny vessels and background noise, as shown in Fig. 4(a). The width of the detected ridge is two pixels under this definition. Since the goal of our method is to robustly and repeatedly detect vessel features, the ‘‘false’’ ridges from the background need to be filtered out. As shown in Table I, both eigenvalues of pixels from background noise are small. Therefore, instead of using the binary ridges directly, the pixels of the ridges are first weighted by their corresponding vesselness values. The obtained measures for ridges are called

$$\begin{aligned} \text{Ridgeness}(x, y, \sigma) = & \text{Vesselness}(x, y, \sigma) \\ & \cdot \text{abs}\{\text{sign}(\nabla I(x + \epsilon u_2, y + \epsilon v_2, \sigma)) \\ & - \text{sign}(\nabla I(x - \epsilon u_2, y - \epsilon v_2, \sigma))\} / 2 \end{aligned} \quad (3)$$

where  $\nabla$  is the gradient operator,  $(u_2, v_2)^T = V_2$  and  $\epsilon = 1.0$  pixel. Up to now, the width of the detected ridge is mostly two pixels. To obtain more accurate single-pixel width ridges, each ridge pixel is further required to be the local maximum in the direction of the eigenvector  $V_2$ . The final definition of our new ridgeness measure is shown as

$$R(\cdot) = \begin{cases} R(\cdot) & \text{if } R(x \pm \epsilon u_2, y \pm \epsilon v_2, \sigma) < R(\cdot) \\ 0 & \text{otherwise} \end{cases} \quad (4)$$

where  $R$  stands for Ridgeness and  $R(\cdot) = \text{Ridgeness}(x, y, \sigma)$ .

As an example, the binary ridge image and the ridgeness image are shown in Fig. 4(a) and (b), respectively. In the ridgeness image, the background noise has been greatly reduced and the ridges now have a single-pixel width. However, in both the binary ridge and ridgeness images, many vessels are broken at branching points, referred to as “broken branching points” for clarity. Therefore, many segmentation-based methods are not able to detect broken branching points. As we show in Section II-C, our branching point detection methods are based on comparing pixels along the circle around the candidate points. Therefore, our method is still able to detect the broken branching points. The ridgeness value on the circle is shown in Fig. 6(b).

### C. Branching Point Detection (RBCT)

Similar to [31], the detected candidates of branching points might contain blobs, specular reflections, branching points, and spurs. This section focuses on how to further distinguish branching points from the others. The major differences are their local structure patterns. One distinctive characteristic of branching points is that they have three or four connecting vessels. Many vessel segmentation methods have been proposed [33] and the branching points can be identified after the vessels are successfully segmented. Compare with those methods, the methods proposed in this paper have the advantage that they do not rely on any image segmentation techniques. Therefore, the proposed method do not need to solve optimization problems required by many image segmentation methods, such as [34]. Inspired by FAST feature point detector [13], we propose to place a circle centered at each candidate point on the ridgeness image and examine the ridgeness value and intensity of each point along the circle to determine whether it is a branching point or not. For clarity, this process of using a circle is termed as “circle test.” Fig. 5 illustrates the idea of the circle test at a branching point. A new method, RBCT, is introduced in this section to detect branching points by performing circle tests on the ridgeness image.

When a circle is placed at the branching point on a ridgeness image, the circle will intersect with the vessels and result in a special “white and black” pattern. Typically, for a bifurcation point, the intersections are three bright points or segments. Note that even though the ridges are single-pixel-width, the intersecting segment of a ridge and a circle might still have more than one pixel. If the intersecting segment is only one pixel, the pixel is defined as a peak. Otherwise, the point with the largest ridgeness in the intersecting segment is defined as a peak. The circle tests on binary ridge image and ridgeness image are shown in

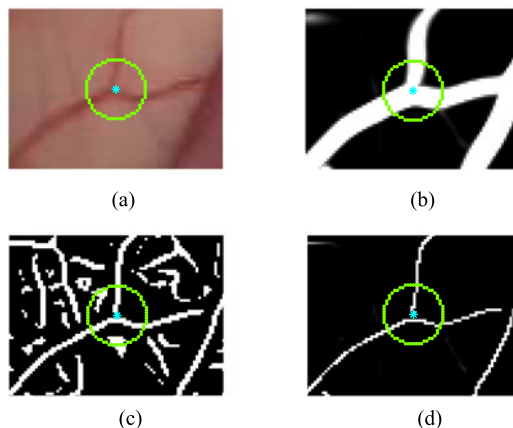


Fig. 5. Typical example of a circle test at a branching point on (a) raw image, (b) vesselness image, (c) binary ridge image, and (d) ridgeness image. As shown, binary ridge image has too much noise. Vessels are thinner on the ridgeness image than on the vesselness image.

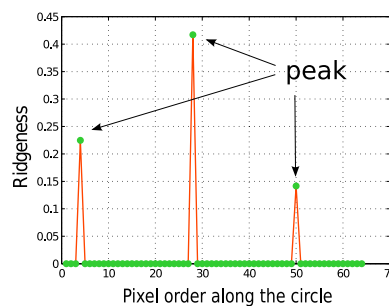


Fig. 6. Ridgeness value of pixels along the circle around a branching point.

Fig. 5(c) and (d). As an example, the ridgeness values of the pixels along the circle are shown in Fig. 6. Note that a similar idea of using peaks for vessel segmentation has been presented in image crawlers [35], [36]. Similar to VBCT [28], multiple tests are employed at each pixel  $p$  on the circle: 1)  $p$  should be bright on the ridgeness image ( $R(p) > R_{\text{peak}}$ ); 2)  $p$  should have similar intensity with the center pixel ( $|I(p) - I(\text{center})| < I_{\text{similar}}$ ); 3) the middle point  $p_m$  of two peaks should be black ( $R(p_m) = 0$ ); and 4) the number of peaks should be three or four. Note that bifurcations and crossing points have three and four peaks, respectively. Among those four tests, as long as one test is failed, the algorithm will exit early to save computation. Because vessels have different widths, to detect as many branching points as possible, multiple circle tests with different radii are employed in RBCT. An example of candidate branching points before and after RBCT is shown in Fig. 7. The pseudo-code of RBCT with one circle test is available in supplemental materials.

### D. Connected Component Labeling and Nonmaximal Suppression

Points that pass the circle test are not the final branching points yet. Depending on the viewing conditions and image resolutions, blood vessels have various widths and it is difficult to mathematically define a unique branching point. The circle test has the locality property that the neighboring pixels have a

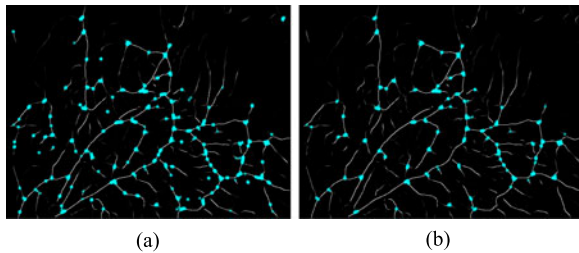


Fig. 7. Candidate branching points (a) before and (b) after RBCT. Those candidates are grouped into connected components.

similar probability of passing the test. Therefore, those points that pass the circle test are grouped into different connected components and each component actually represents one branching point. The eight-neighbor definition is used here to label the connected components with the two-pass algorithm [37]. After each connected component has been identified, its center is defined as the location of the branching point.

Different from corners that can be very close to each other, branching points are much more sparse and are usually far from each other. We further require that the distance between any two branching points should be larger than or equal to a predefined minimum distance. The minimum distance of branching points is determined by multiple factors, such as the resolutions of the images, the tissue-to-camera distances, and so on. Based on the collected datasets as discussed in Section III-A, this minimum distance is set to be 11 pixels ( $\text{distance}_{\min} = 11$ ) in this paper. The minimum distance is ensured by nonmaximal suppression with a  $23 \times 23$  window. Since a large connected component is more robust than a small one, the number of points in each connected component is chosen as the score of the corresponding branching point and used in the nonmaximal suppression process.

### E. Branching Segment Detection (RBSD)

In this section, we describe the procedure of vessel tracing contained in RBSD. Since branching segment detection starts and ends at branching points, our algorithm starts from each branching point and initiates a vessel tracing process for each of its corresponding vessels. The vessel tracing process is the core of the branching segment detection, and our algorithm is based on the binary mask of vessels, which is obtained by thresholding the ridgeness image and is referred to as “ridge mask.” The ridge mask has a single-pixel width in most areas, except the specular reflections. The following discussion is based on the binary ridge mask. The vessel tracing process is recursive and stops under two conditions. First, another branching point is within a five-pixel radius ( $\text{radius}_{\text{BS}} = 5$ ), which means a branching segment has been detected. Second, there are no unvisited ridge pixels, which results in a half branching segment.

Three key points need to be determined during the vessel tracing process: the starting point, the next point, and the ending point. First, the detected position of a branching point is not directly used as the starting point, because the broken branching point may not be on the vessel. The three or four peaks from the

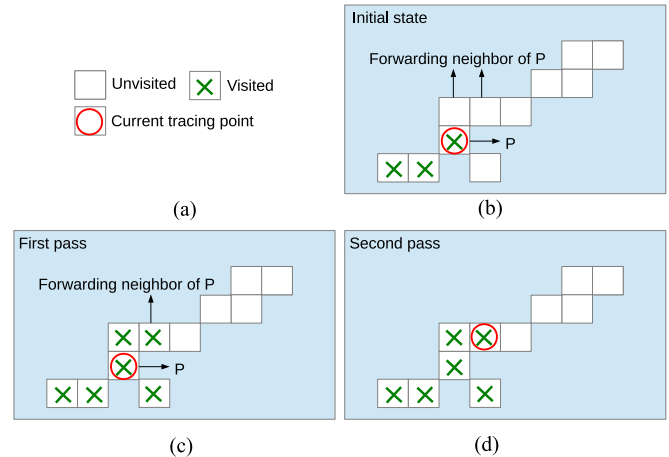


Fig. 8. Illustration of the two-pass test vessel tracing process. (a) Explanation of labels, (b) initial state, (c) state after first pass, (d) state after second pass.

circle test of each branching point are, therefore, chosen as the starting points for tracing.

To determine the next point and the ending point, some special points on the ridge mask have to be defined for clarity. A “forwarding point” is a point that is white on the ridge mask and has at least one white unvisited neighbor (under eight neighbor). If a point,  $P$ , has a neighbor that is a forwarding point, this neighbor is called “forwarding neighbor” of point  $P$ . One example of forwarding point and forwarding neighbor is given in Fig. 8(b). The key observation of our vessel tracing is as follows: given the current tracing point  $P$ , after marking  $P$ ’s neighbors as visited, if  $P$  still has forwarding neighbors, we conclude that all these forwarding neighbors are along the vessel and in front of  $P$ .

Based on this observation, the following two-pass tracing algorithm is applied in each iteration. The first pass is to collect all unvisited white neighbors of the current tracing point and mark them as visited. The second pass is to find all forwarding neighbors. If at least one forwarding neighbor is found, the next point can be chosen as either one of them; otherwise, this is the end of the current vessel tracing process. Regarding the ending point, if no branching point is found at the end of the tracing, the last point of the vessel tracing process is chosen as the ending point; otherwise, another branching point is found and is chosen as the ending point. The process of two-pass vessel tracing is illustrated in Fig. 8. The detected branching segments (green) and half branching segments (blue) are shown in Fig. 9(b) as an example. The pseudo-code of the branching segment detection is given in supplemental materials.

### F. Computational Analysis and Run Time Results

Since RBCT is a part of RBSD, this section focuses on the computational analysis of RBSD. There are three main components in the calculation of RBSD: ridgeness, circle test, and vessel tracing. First, based on (3) and (4), it can be seen that, the calculation of vesselness accounts for the main computation of ridgeness. Note that 2-D version of Frangi vesselness with three image levels is used in this paper. Its calculation contains three Gaussian convolutions for each image level to obtain

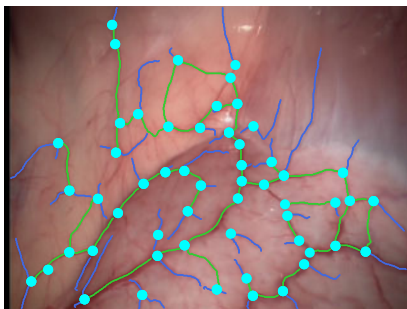


Fig. 9. The illustration of those vessel features detected by RBSD: branching segments (green), half branching segments (blue), and branching points (cyan dots).

TABLE II  
RUN TIME OF DIFFERENT STEPS IN RBSD

Circle test	Labeling	Suppression	Vessel tracing
0.562(s)	0.027(s)	0.088(s)	0.062(s)

“Labeling” Represents Connected Component Labeling.  
“Suppression” represents Nonmaximum suppression. “S” stands for second.

Hessian matrix and the calculation of eigenvalues in the  $2 \times 2$  Hessian matrix for each pixel. Those calculations have been used and analyzed in [16], [18], and [38] and can achieve real-time speed with proper implementation. Second, circle tests are performed on each candidate branching point, which is usually less than 1% of the total number of pixels. Typically, one circle test scans 64 pixels along the circle (11-pixel radius) and less than six computer instructions are executed to scan one pixel. Third, the proposed vessel tracing algorithm visits each ridge point one time, at most, to detect all branching segments and half branching segments.

The run-time tests of different steps in RBSD are performed on a Intel core i5 CPU 650 (3.20 GHz) with 4.00 GB RAM. The test data contains images with resolution  $640 * 480$  from an *in vivo* MIS dataset (scene7 from the public Hamlyn dataset [39] as introduced in Section III-A). The proposed methods have been implemented using MATLAB. The average run time of different steps for one image are reported in Table II. The results with unoptimized MATLAB implementation in Table II show that the proposed methods are fast and can potentially achieve real-time speed with proper implementation, such as C/C++. In addition, the proposed methods can be faster by exploiting graphics processing unit (GPU), since the circle tests can be independently executed.

### III. EXPERIMENTS AND RESULTS

In this section, *in vivo* experiments were designed to evaluate the performances of the proposed vessel feature detectors. Many state-of-the art branching point detectors [40], [41], vessel detection methods [33], [42], general feature point detectors have been proposed in the community. Among them, the following feature detectors were chosen based on the reports in [13] and

TABLE III  
PARAMETERS OF STATE-OF-THE-ART FEATURE DETECTORS USED IN THIS PAPER

Procedure	Parameters
AFD	sigma = 1.5, cornerness threshold = 0.2, step=1.44, and number of scales = 7
DoG	peak threshold = 0.008, edge threshold = 10
Hessian affine	peak threshold = 0.0008, edge threshold = 10
FAST	intensity threshold = 14 (range [0 255])
Sofka	likelihood ratio threshold = 1.0

[17] and the availability of codes: VBCT [28], AFD [17], DoG [19], Hessian affine [18], [31], FAST [14], and likelihood ratio vesselness (referred to as “Sofka” in this paper) [42]. Note that VBCT, RBCT, and Sofka were branching point detectors. RBSD was a branching segment detector. The rest of them were not specifically designed for vessel images and were referred to as “general feature point detectors” in this paper. Those general feature point detectors extracted different information from a given image: intensity (FAST), first derivatives (AFD), and second derivatives (Hessian affine, DoG). The implementations of Hessian affine and DoG from VLFeat library [43] were adopted in this paper. The parameters of the aforementioned methods were chosen based on the datasets used in this paper and the suggestions from the corresponding papers. Those parameters were shown in Table III and were fixed in all the experiments.

The parameters used in RBCT and RBSD were selected based on their performance on the datasets (see Section III-A) used in this paper. During the detection of the branching point candidates, the following threshold values produced reasonable amount of candidates and were able to detect most branching points:  $\lambda_{1\min} = 0.05$ ,  $R_{\min} = 0.01$ . In the calculation of the Vesselness, the following values were adopted based on the suggestions of [29]:  $\sigma = \{3, 4, 5\}$ ,  $\beta = 0.5$ , and  $c = 15$ . In the process of circle test, the threshold values were set as:  $R_{\text{peak}} = 0.01$ ,  $I_{\text{similar}} = 0.03$  (intensity range [0 1]), which filtered out high percentage of outliers and kept most branching points. Two circle tests were shown enough to detect most branching points in our datasets and their radii were 7 and 5 pixels, respectively.

The objective of the experiments is to evaluate, in MIS images, how distinctive vessel features detected by RBCT and RBSD are compared with general feature points (corners and blobs). Note that RBCT is a part of RBSD. They are treated as a unit and are compared with the others in all the experiments. Branching points, branching segments, corners, and blobs are different types of features and they have different densities in the images. The minimum distances of branching points, branching segments, and general feature points were defined as 11 pixels, 0 pixel, and 1 pixel, respectively. To have a consistent comparison, we applied nonmaximum suppression with 11-pixel radius for all the methods, including branching segments so that the minimum distance between any two feature points was at least 11 pixels. To apply nonmaximum suppression, scores indicating the significance of feature points, such as cornerness scores, should be provided. Note that no scores were provided

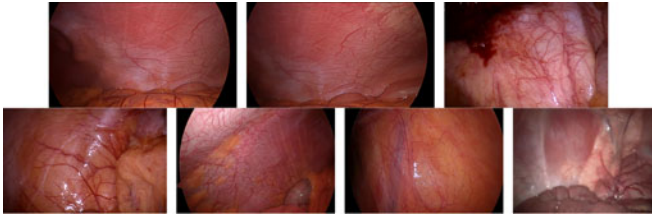


Fig. 10. Sample images of the seven *in vivo* video clips.

for points from DoG, to run the nonmaximum suppression, all points were considered to be equally important by assigning the same cornerness score.

#### A. In Vivo Datasets and Ground Truths

Our datasets contained seven *in vivo* video clips representing different imaging conditions in different surgeries. Sample images were shown in Fig. 10. Those videos were taken during the laparoscopic colon surgeries of three different patients. They were named in the order from scene1 to scene7. In scene1, scene2, scene5, and scene6, the laparoscope faced toward the abdominal wall and was moved along the abdominal wall. Because the abdomen was insufflated in MIS, those areas of the abdominal wall were approximately flat. Scene3 and scene4 were small flat tissue surfaces within the anterior pelvis, where the uterus was removed. In those two video clips, the stereoscope rotated and zoomed in and out on top of the scenes. Scene7 was from the public Hamlyn dataset [39], where the endoscope was moved to explore the scene.

One important property of a feature point detector is that the same scene point can be detected repeatedly from different viewpoints. Homography mappings have been widely used in the literature to measure this property. To have global homography mappings, it is required that either the scenes are mostly planar or the camera is rotated around its center. The above datasets have been specially chosen in order to have global homography mappings: the first six scenes are mostly planar, and in the seventh scene, the camera is mainly rotated around its center.

The ground-truth homography mappings for each pair of images in each scene were obtained by manually selecting point correspondences between the image pairs. In each scene, one frame was chosen as the reference image and the planar area of the scene was selected as the region of interest. Each image is coupled with the reference image to form image pairs. In each pair of images, 20 well-distributed point correspondences between the reference image and the others were manually selected by experienced observers. One example of the manually selected ground truth is shown in Fig. 11. The selected correspondences were later used to calculate the ground-truth homography mappings following the methods used in [14] and [18]. Due to the similarity between successive frames and the large efforts required by the manual point selection, those video clips were uniformly sampled to reduce the manual work. The number of selected frames for each video clip is shown in the fifth column of Table IV. The errors of homography mappings

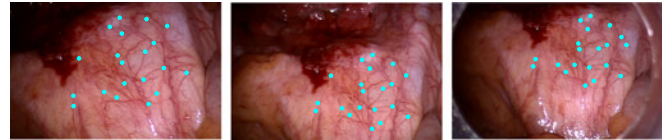


Fig. 11. Illustration of selected ground-truth point correspondences (cyan) across different views in scene 3.

TABLE IV  
SUMMARY OF DATASETS USED IN THIS PAPER

Datasets	Source	Homo. type	Length	Frame num.	Resolution	Homo. error
Scene1	patient1	planar	3s	50	1280 × 720	1.6 ± 0.8
Scene2	patient1	planar	3s	50	1280 × 720	1.5 ± 0.7
Scene3	patient2	planar	5s	53	1240 × 800	2.0 ± 1.0
Scene4	patient2	planar	3s	45	1240 × 800	2.0 ± 1.0
Scene5	patient3	planar	8s	22	720 × 480	1.7 ± 0.9
Scene6	patient3	planar	8s	14	720 × 480	1.6 ± 0.7
Scene7	[39]	rotation	23s	49	640 × 480	1.9 ± 0.9

“Planar” means the scene is planar. “Rotation” represents that the camera motion is rotation only. “Frame num.” indicates how many frames are kept after sampling. “Homo. error” denotes the average errors of the ground-truth homography mappings. The unit of Homographic error is pixel.

for each scene are reported in the last column of Table IV. Note that the errors of homography mappings indicate whether it is valid or not to use those mappings for generating ground-truth feature point positions.

Note that the common accuracy of homography mappings used for general feature point detectors is 1.5 pixels [13], [16], which is more accurate than that of our homography mappings as shown in Table IV. This is because the constraints in the MIS environment make it extremely difficult to obtain the exact homography mapping between two MIS images. As shown in the last column of Table IV, the homography errors are smaller than 3 pixels. With inaccurate homography mapping, each point in the first image is mapped to a 3-pixel-radius disk in the second image. Since those disks should not overlap in the second image, the minimal distance of any two feature points should be larger than 6 pixels. Our feature points have minimal distance of 11 pixels, which are larger than 6 pixels. Therefore, the obtained homography mappings are accurate enough.

#### B. Repeatability and Number of Points

The repeatability and total number of detected points are two widely used measures to evaluate the performance of feature detectors [13], [16]. To this end, repeatability is defined as the percentage of points that are detected in images from different viewpoints. Because there is noise in the detected positions of the feature points, two points  $x_1, x_2$  are defined to correspond to each other if  $|x_2 - H \cdot x_1| < \delta$ , where  $H$  is the homography mapping and  $\delta$  is a predefined threshold. Based on the accuracies of the ground-truth homography mappings shown in Table IV,  $\delta$  is set to be 3.5 pixels for all feature point detectors. Note that this is different from [13], [16], and [18], where the  $\delta$  is about

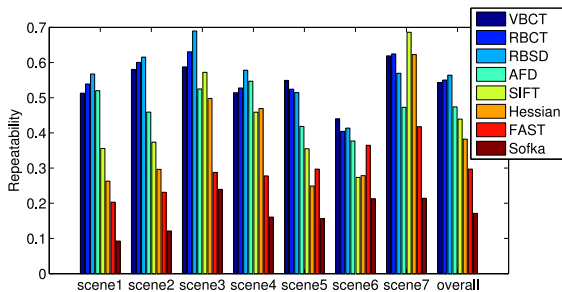


Fig. 12. Repeatability scores of different methods in the seven scenes. The overall performance is shown on the right. The details of the repeatability scores for each frame in each scene are displayed as repeatability curves and have been included in the supplemental materials.

1.5 pixels. In this paper, the repeatability is defined as

$$\text{repeatability} = \frac{m}{\min\{n_1, n_2\}} \quad (5)$$

where  $m$  is the number of points detected in both images,  $n_1$  is the number of points detected in the first image, and  $n_2$  is the number of points detected in the second image, whose corresponding points are also visible in the first image. We note that the repeatability measure might be biased against those detectors that detect more points.

The repeatability of different feature detectors on the seven scenes is shown in Fig. 12. The overall performance for each method is displayed at the right in Fig. 12. As shown, vessel feature detectors outperform the general feature point detectors having the highest average repeatability scores under camera translation and rotation. The major reason is that the general feature points are small in scale and less distinctive under large camera motions. On the other hand, vessels are among the most distinctive structures in MIS images and are resistant to large camera motions. Note that FAST does not perform as well as expected. One possible reason is that comparing with general images, the endoscopic images are more noisy due to the special camera sensor and imaging environment in MIS. As pointed out in [13], FAST is designed to compare as few pixels as possible, and is therefore, less robust toward the noises in MIS images. In scene7, the camera is mainly rotated around the optical axis and the camera barely changes its viewpoint. The images in scene7 have small perspective changes, and therefore, all feature detectors have better repeatability scores.

The number of points detected by the state-of-the-art feature point detectors is shown in Fig. 13. The average number of points detected by each method is displayed on the right in Fig. 13. Due to the sparsity of branching points, the number of branching points is the fewest among all methods. On the other hand, RBSD is essentially curve-segment detector, which detects not only the branching points but also the points along the vessel segment. Therefore, RBSD usually detects much more points than general point detectors. We notice that it is unfair to compare the number of points detected by different types of feature detectors. Therefore, the number of points detected by RBSD is separately given in Table V. Reporting the numbers of points detected by RBCT and RBSD is to verify that the small number of available branching points can be compensated by the large number of pixels detected along the vessel provided

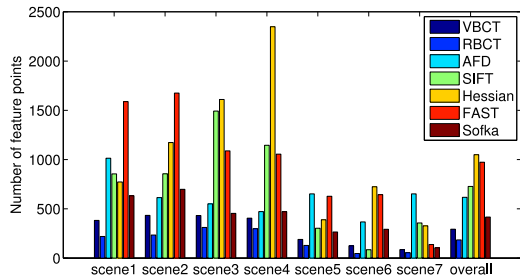


Fig. 13. Number of feature points detected by different feature point detectors in the seven scenes. The overall performance is shown on the right. Note that RBSD is a branching segment detector, which is different from general point detector and usually detects much more points as shown in Table V.

TABLE V  
TOTAL NUMBER OF POINTS IN ALL BRANCHING SEGMENTS  
DETECTED BY RBSD

S1	S2	S3	S4	S5	S6	S7	Average
5661	6296	5749	5430	2204	1098	1177	3945

“S” stands for scene.

by RBSD. In addition, vessel features can be combined with general feature points to extract more rich information from the images.

It is useful to see how many human-recognizable branching points can be detected by the proposed branching point detector. Four representative images are selected from each of the seven scenes and the human-recognizable branching points are manually selected by experienced human subjects. For each image, the sets of manually selected branching points and the automatically detected ones are denoted as  $S_1$  and  $S_2$ , respectively. The coverage is defined as the percentage of ground-truth branching points that is automatically detected:  $|S_1 \cap S_2|/|S_1|$ , where  $\cap$  represents intersection of two point sets. The average coverage for RBCT is 70%, which means, in average, 70% out of human-recognizable branching points is automatically detected.

### C. Patch Matching Correctness

One target application of branching point detection is endoscope localization and mapping, in which both feature point detection and matching are crucial. In this section, a correlation-matching-based patch search process from the parallel tracking and mapping (PTAM), called “fixed range image search” [44], is adopted, and different feature point detectors are applied and compared. Since the goal here is to compare different feature detectors only, to be fair, the same feature matching method needs to be used for all feature detectors. Note that SIFT descriptor is not used for DoG during the point matching process. In the patch search process, a high matching correctness indicates that the feature point detector has high repeatability and the image patches extracted are distinctive for matching purpose. The patch search procedure takes the first image as the current frame and assumes the second image as the frame that has been saved in the endoscope localization system. The feature points of the second image are treated as known to the system and are called

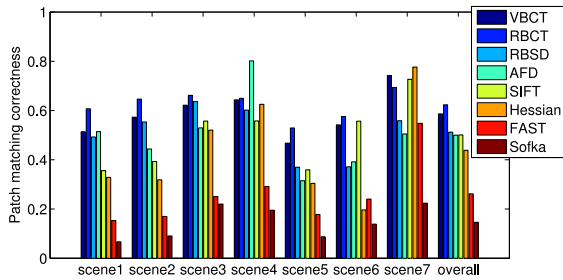


Fig. 14. Patch matching correctness of different methods in the seven scenes. The overall performance is shown on the right.

“map points” [44]. The goal is to identify those map points in the current frame.

The patch search process contains a couple of steps. First, since only the patch search process from PTAM is employed rather than the whole system, the temporal information from previous frames is preserved by defining a search area in the current frame for each map point. For each map point  $P$  in the saved frame, its corresponding point  $Q$  in the current frame as ground truth can be obtained through homography mapping. The search area of  $P$  in the current frame is a disk centered at  $Q$ , whose radius is  $1/20$  of the image width. Second, the feature points in the current frame that are within this fixed range are chosen and referred to as the nearby points. The  $21 \times 21$  local patch of each nearby point is compared with the same size local patch of  $P$ . Third, similar to [44], an affine warping, which is obtained from the ground-truth homography mapping, is applied to the patch of  $P$  to take care of the view-point change. After warping, zero-mean sum of squared distance (ZSSD) is calculated for each pair of patches. Finally, a nearby point is considered as a match if its ZSSD value is the minimum and the value is smaller than the predefined threshold of 0.02 in this paper for the normalized intensity range  $[0, 1]$ . A match  $Q'$  is defined to be correct if  $|Q' - Q| < 3.5$  pixels. The correctness of the SSD matching is defined to be the ratio of the number of correct matches over the number of total matches.

The patch matching results are given in Fig. 14. Vessel features perform better than the general features again, which further verifies the distinctiveness of vessel features. In patch matching, VBCT and RBCT have higher matching correctness scores than RBSD. This is because the patterns of branching points are more distinctive than the patterns of vessel points (except the endpoints) in branching segments. Note that in scene4, the patch matching correctness of AFD is significantly better than all the others. One reason is that the specular reflections are strong and abundant in scene4. Since our homography mappings are not accurate enough, the movements of the points on the specular reflections cannot be captured. Therefore, specular reflections are mistreated as fixed textures and those points on the boundaries of specular reflections are misclassified as correct matches. One example of patch matching result with RBCT is shown in Fig. 15.

#### IV. CONCLUSION AND FUTURE WORK

It is well known that feature extraction in MIS images is difficult due to the special imaging environment. The existence of

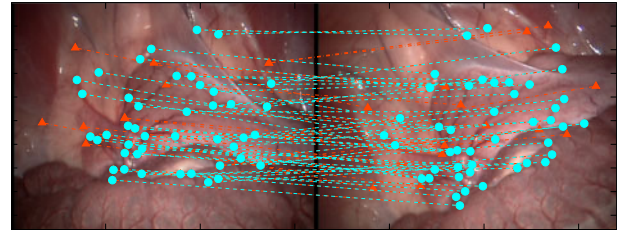


Fig. 15. One example of correlation-based patch matching using “fixed range image search” [44] with feature detector RBCT. Matches with error less than 3.5 pixels are classified as correct matches (cyan dots). The others are classified as incorrect matches (red triangles). The images are from the seventh scene. Note that the detected branching points that are not matched by the correlation-based patch matching method are not displayed.

abundant blood vessels in intraabdominal MIS images provides a solution to overcome this problem. This paper proposes to extract branching segments as features and has quantitatively verified their distinctiveness. Moreover, the vessel features can be combined with general feature points since they extract different structures in the images. Therefore, RBCT and RBSD offer researchers new types of distinctive features for endoscopic image analysis. The evaluation codes, the codes of RBCT and RBSD, and the datasets used in this paper are available online at <http://rpal.cse.usf.edu/project1/index.html>.

The distinctive vessel features can have many applications for endoscopic images. When stereoscope is available, as in *da Vinci* system, those detected vessel features can be matched in stereo images using traditional correlation-matching methods [6] and the 3-D structures of those vessels can be recovered. Similarly, in visual SLAM systems, vessel features can be detected in different frames and matched using correlation-based patch matching methods [44]. The matching of vessel features in different views allows endoscope to localize itself and also enables the recovery of the 3-D vascular structures after the endoscope poses are successfully calculated. More importantly, those 3-D vessels recovered from different views can be merged together to obtain a large 3-D vessel network, which provides a very good 3-D structure of the whole abdominal area and will be very beneficial for the coregistration with preoperative CT data. The intraoperative structure recovered by the endoscope also sheds light on solving the difficult deforming or dynamic coregistration problems [3], [12].

In stereo reconstruction and visual SLAM, vessel features can be similarly matched with the traditional correlation-based patch matching methods. To better exploit the properties of vessel features, in our future work, we plan to design a specialized matching method for vessel features, which can take advantage of the branch and vessel directions.

Due to the nature of large-scale features of branching points, the current location error of automatic localization of matching points is about  $1.6 \pm 0.7$  pixels. This error is larger than general feature point detectors, which typically achieve 1-pixel accuracy. The larger error of branching points introduces uncertainty to its applications, such as pose estimation and 3-D reconstruction. In the future, we will further refine the branching point location accuracy based on the local neighbor information.

In order to further speed up the circle test in RBCT, one future research direction is to add early termination so that unnecessary

computations can be avoided. Another research direction is to incorporate the supervised learning techniques [13] into vessel feature detection.

## REFERENCES

- [1] P. Mounthey *et al.*, "A probabilistic framework for tracking deformable soft tissue in minimally invasive surgery," in *Proc. Int. Conf. Med. Image Comput. Comput.-Assisted Intervention*, 2007, pp. 34–41.
- [2] R. Richa *et al.*, "Efficient 3D tracking for motion compensation in beating heart surgery," in *Proc. Int. Conf. Med. Image Comput. Comput.-Assisted Intervention*, 2008, pp. 684–691.
- [3] M. C. Yip *et al.*, "Tissue tracking and registration for image-guided surgery," *IEEE Trans. Med. Imag.*, vol. 31, no. 11, pp. 2169–2182, Nov. 2012.
- [4] P. Mounthey and G.-Z. Yang, "Soft tissue tracking for minimally invasive surgery: Learning local deformation online," in *Proc. Int. Conf. Med. Image Comput. Comput.-Assisted Intervention*, 2008, vol. 11, pp. 364–372.
- [5] B. Lin, Y. Sun, and X. Qian, "Thin plate spline feature point matching for organ surfaces in minimally invasive surgery imaging," *Proc. SPIE*, vol. 867112, pp. 867112-1–867112-7, 2013.
- [6] D. Stoyanov *et al.*, "Real-time stereo reconstruction in robotically assisted minimally invasive surgery," in *Proc. Int. Conf. Med. Image Comput. Comput.-Assisted Intervention*, 2010, pp. 275–282.
- [7] L. Maier-Hein *et al.*, "Optical techniques for 3D surface reconstruction in computer-assisted laparoscopic surgery," *Med. Image Anal.*, vol. 17, no. 8, pp. 974–996, 2013.
- [8] B. Lin, *et al.*, "Simultaneous tracking, 3D reconstruction and deforming point detection for stereoscope guided surgery," in *Augmented Reality Environments for Medical Imaging Computer-Assisted Intervention*, vol. 8090. Berlin, Germany: Springer, 2013, pp. 35–44.
- [9] P. Mounthey and G.-Z. Yang, "Motion compensated slam for image guided surgery," in *Proc. Int. Conf. Med. Image Comput. Comput.-Assisted Intervention*, 2010, pp. 496–504.
- [10] D. Mirotu *et al.*, "A system for video-based navigation for endoscopic endonasal skull base surgery," *IEEE Trans. Med. Imag.*, vol. 31, no. 4, pp. 963–976, Apr. 2012.
- [11] A. L. Anderson *et al.*, "Virtually transparent epidermal imagery (VTEI): On new approaches to in vivo wireless high-definition video and image processing," *IEEE Trans. Biomed. Circuits Syst.*, vol. 7, no. 6, pp. 851–860, Dec. 2013.
- [12] S. Ding *et al.*, "Tracking of vessels in intra-operative microscope video sequences for cortical displacement estimation," *IEEE Trans. Biomed. Eng.*, vol. 58, no. 7, pp. 1985–1993, Jul. 2011.
- [13] E. Rosten and T. Drummond, "Machine learning for high-speed corner detection," in *Proc. Eur. Conf. Comp. Vis.*, vol. 1, 2006, pp. 430–443.
- [14] E. Rosten *et al.*, "Faster and better: A machine learning approach to corner detection," *IEEE Trans. Pattern Anal. Mach. Intell.*, vol. 32, no. 1, pp. 105–119, Jan. 2010.
- [15] C. Harris and M. Stephens, "A combined corner and edge detector," in *Proc. 4th Alvey Vis. Conf.*, 1988, pp. 147–151.
- [16] K. Mikolajczyk and C. Schmid, "Scale & affine invariant interest point detectors," *Int. J. Comput. Vis.*, vol. 60, no. 1, pp. 63–86, 2004.
- [17] S. Giannarou *et al.*, "Probabilistic tracking of affine-invariant anisotropic regions," *IEEE Trans. Pattern Anal. Mach. Intell.*, vol. 35, no. 1, pp. 130–143, Jan. 2013.
- [18] K. Mikolajczyk *et al.*, "A comparison of affine region detectors," *Int. J. Comput. Vis.*, vol. 65, no. 1/2, pp. 43–72, 2005.
- [19] D. G. Lowe, "Distinctive image features from scale-invariant keypoints," *Int. J. Comput. Vis.*, vol. 60, no. 2, pp. 91–110, 2004.
- [20] H. Bay *et al.*, "SURF: Speeded up robust features," in *Proc. Eur. Conf. Comput. Vis.*, 2006, pp. 404–417.
- [21] G. Puerto-Souza and G. Mariottini, "Hierarchical multi-affine (HMA) algorithm for fast and accurate feature matching in minimally-invasive surgical images," in *Proc. IEEE/RSJ Int. Intell. Robots Syst. Conf.*, 2012, pp. 2007–2012.
- [22] G. Puerto-Souza and G.-L. Mariottini, "Wide-baseline dense feature matching for endoscopic images," in *Image and Video Technology*, (Lecture Notes in Computer Science), vol. 8333. Berlin, Germany: Springer, 2014, pp. 48–59.
- [23] G. Puerto-Souza and G. Mariottini, "Adaptive multi-affine (ama) feature-matching algorithm and its application to minimally-invasive surgery images," in *Proc. Int. Conf. Med. Image Comput. Comput.-Assisted Intervention*, Oct. 2012, pp. 625–633.
- [24] G. Puerto-Souza and G.-L. Mariottini, "A fast and accurate feature-matching algorithm for minimally-invasive endoscopic images," *IEEE Trans. Med. Imag.*, vol. 32, no. 7, pp. 1201–1214, Jul. 2013.
- [25] B. Lin *et al.*, "Dense surface reconstruction with shadows in MIS," *IEEE Trans. Biomed. Eng.*, vol. 60, no. 9, pp. 2411–2420, Sep. 2013.
- [26] D. Stoyanov, "Surgical vision," *Ann. Biomed. Eng.*, vol. 40, pp. 332–345, 2012.
- [27] E. Rosten and T. Drummond, "Fusing points and lines for high performance tracking," in *Proc. Int. Conf. Comput. Vis.*, 2005, vol. 2, pp. 1508–1515.
- [28] B. Lin *et al.*, "Vesselness based feature extraction for endoscopic image analysis," in *Proc. Int. Symp. Biomed. Imag.*, 2014, pp. 1295–1298.
- [29] A. F. Frangi *et al.*, "Multiscale vessel enhancement filtering," in *Proc. Int. Conf. Med. Image Comput. Comput.-Assisted Intervention*, 1998, pp. 130–137.
- [30] L. Shi *et al.*, "Quaternion color curvature," in *Proc. IS&T Color Imag. Conf.*, 2008.
- [31] D. Baboiu and G. Hamarneh, "Vascular bifurcation detection in scale-space," in *Proc. IEEE Workshop Math. Meth. Biomed. Image Anal.*, 2012, pp. 41–46.
- [32] J. Staal *et al.*, "Ridge-based vessel segmentation in color images of the retina," *IEEE Trans. Med. Imag.*, vol. 23, no. 4, pp. 501–509, Apr. 2004.
- [33] K. Krissian *et al.*, "Model-based multiscale detection of 3D vessels," in *Proc. Comput. Vis. Pattern Recog.*, Jun. 1998, pp. 722–727.
- [34] E. Bae *et al.*, "A fast continuous max-flow approach to non-convex multi-labeling problems," in *Efficient Algorithms for Global Optimization Methods in Computer Vision*. Berlin, Germany: Springer, 2014, pp. 134–154.
- [35] C. McIntosh and G. Hamarneh, "Vessel crawlers: 3D physically-based deformable organisms for vasculature segmentation and analysis," in *Proc. Comput. Vis. Pattern Recog.*, Jun. 2006, vol. 1, pp. 1084–1091.
- [36] G. Hamarneh and C. McIntosh, "Deformable organisms for medical image analysis," in *Deformable Models: Biomedical and Clinical Applications* (Topics in Biomedical Engineering International Book Series). New York, NY, USA: Springer, 2007, pp. 387–443.
- [37] L. G. Shapiro and G. Stockman, *Computer Vision*, 1st ed. Upper Saddle River, NJ, USA: Prentice Hall, 2001.
- [38] J. Shi and C. Tomasi, "Good features to track," in *Proc. Comput. Vis. Pattern Recog.*, 1994, pp. 593–600.
- [39] S. Giannarou *et al.* (2014). Hamlyn centre laparoscopic / endoscopic video datasets. [Online]. Available: <http://hamlyn.doc.ic.ac.uk/vision/>
- [40] M. Zhao and G. Hamarneh, "Bifurcation detection in 3D vascular images using novel features and random forest," in *Proc. IEEE Int. Symp. Biomed. Imag.*, 2014, pp. 421–424.
- [41] M. M. G. Macedo *et al.*, "A center-line based estimator of vessel bifurcations in angiography images," *Proc. SPIE*, pp. 86 703K-1–86 703K-7, 2013.
- [42] M. Sofka and C. V. Stewart, "Retinal vessel centerline extraction using multiscale matched filters, confidence and edge measures," *IEEE Trans. Med. Imag.*, vol. 25, no. 12, pp. 1531–1546, Dec. 2006.
- [43] A. Vedaldi and B. Fulkerson, "—An open and portable library of computer vision algorithms," in *Proc. ACM Int. Conf. Multimedia*, 2010, pp. 1469–1472.
- [44] G. Klein and D. W. Murray, "Parallel tracking and mapping for small AR workspaces," in *Proc. Int. Symp. Mixed Augmented Reality*, 2007, pp. 225–234.

Authors' photographs and biographies not available at the time of publication.